

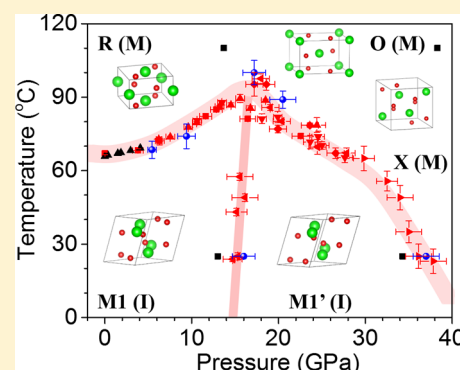
## Pressure–Temperature Phase Diagram of Vanadium Dioxide

Yabin Chen,<sup>†</sup> Shuai Zhang,<sup>‡</sup> Feng Ke,<sup>§</sup> Changhyun Ko,<sup>†</sup> Sangwook Lee,<sup>†</sup> Kai Liu,<sup>||</sup> Bin Chen,<sup>§</sup> Joel W. Ager,<sup>†,⊥</sup> Raymond Jeanloz,<sup>‡</sup> Volker Eyert,<sup>#</sup> and Junqiao Wu<sup>\*,†,⊥</sup><sup>†</sup>Department of Materials Science and Engineering, <sup>‡</sup>Department of Earth and Planetary Science, University of California, Berkeley, California 94720, United States<sup>§</sup>Center for High Pressure Science and Technology Advanced Research, Shanghai 201203, China<sup>||</sup>State Key Laboratory of New Ceramics and Fine Processing, School of Materials Science and Engineering, Tsinghua University, Beijing 100084, China<sup>⊥</sup>Materials Sciences Division, Lawrence Berkeley National Laboratory, Berkeley, California 94720, United States<sup>#</sup>Materials Design SARL, 92120 Montrouge, France

## Supporting Information

**ABSTRACT:** The complexity of strongly correlated electron physics in vanadium dioxide is exemplified as its rich phase diagrams of all kinds, which in turn shed light on the mechanisms behind its various phase transitions. In this work, we map out the hydrostatic pressure–temperature phase diagram of vanadium dioxide nanobeams by independently varying pressure and temperature with a diamond anvil cell. In addition to the well-known insulating M1 (monoclinic) and metallic R (tetragonal) phases, the diagram identifies the existence at high pressures of the insulating M1' (monoclinic, more conductive than M1) phase and two metallic phases of X (monoclinic) and O (orthorhombic, at high temperature only). Systematic optical and electrical measurements combined with density functional calculations allow us to delineate their phase boundaries as well as reveal some basic features of the transitions.

**KEYWORDS:** VO<sub>2</sub>, phase transition, phase diagram, hydrostatic pressure, diamond anvil cell



Vanadium dioxide (VO<sub>2</sub>), as a prototype of strongly correlated electron materials, is of great interest in condensed matter physics as well for device applications.<sup>1–3</sup> The electron correlation interplaying with lattice stabilizes a very rich phase diagram of VO<sub>2</sub> that consists of many phases with distinct structures and electronic properties. Transitions between these phases can be driven by temperature, photoexcitation, hydrostatic pressure, uniaxial stress, or electrical gating.<sup>1,4–12</sup> For example, the well-known, insulating M<sub>1</sub> (monoclinic, space group *P2<sub>1</sub>/c*) phase transforms to the metallic R (tetragonal, *P4<sub>2</sub>/mmm*) phase at 68 °C under ambient pressure.<sup>1</sup> This M<sub>1</sub>–R transition can also be driven by hydrostatic pressure<sup>6</sup> or uniaxial compression.<sup>4</sup> The application of hydrostatic pressure is a clean and powerful way to tune the lattice and electronic degrees of freedom. Hydrostatic pressure applied via a diamond anvil cell (DAC) has also been able to drive the M<sub>1</sub> phase to another isostructural, more conductive M<sub>1</sub>' phase, and finally a new metallic X (monoclinic) phase at room temperature, and to drive the metallic R phase to new metallic O and X phases at 383 K.<sup>9</sup> A pressure–temperature phase diagram has been proposed for VO<sub>2</sub>.<sup>8</sup> However, this phase diagram with three regions of M<sub>1</sub>, M<sub>X</sub>, and R is largely schematic, and their phase boundaries, especially at high pressures, are unclear, undefined, and unsubstantiated with experimental data. In this work, we establish a clear hydrostatic

pressure–temperature (*P*–*T*) phase diagram for VO<sub>2</sub>, quantitatively delineating the phase boundaries between the M<sub>1</sub>, M<sub>1</sub>', R, O, and X phases, and provide comparisons to first-principles calculations.

The phase transitions were identified within a heated DAC by various techniques, including Raman spectroscopy, optical reflectance, and electrical transport. The VO<sub>2</sub> nanobeams used in this work were grown using a vapor transport method.<sup>13</sup> They typically have a flat surface and small (<1 μm) thickness, and exhibit a single-domain, sharp metal–insulator transition (MIT) at *T*<sub>MIT</sub> = 68 °C, with a narrow hysteresis. All high-pressure experiments were performed in a four-post DAC with 300 μm culet size (see Supporting Information). The pressure-transmitting medium was a mixture of methanol–ethanol (4:1) and Daphne 7373, for Raman and electrical measurements, respectively. A quasi four-probe geometry was used for the electrical measurements using Pt foil as electrodes, and the microdevice fabrication method can be found elsewhere.<sup>14</sup> High temperatures were realized by heating the DAC in a water bath or with heating belts. The pressure was calibrated with the standard method of ruby photoluminescence.<sup>15</sup> The temper-

Received: January 17, 2017

Revised: March 6, 2017

Published: March 7, 2017

ature was measured with a thermocouple placed very close to the gasket chamber. Theoretical calculations were performed within the framework of density functional theory (DFT). Electron–electron exchange and correlation effects were described by the generalized gradient approximation with the Perdew–Burke–Ernzerhof (PBE)<sup>16</sup> functional plus Hubbard  $U$ .<sup>17</sup> The density-functional or Kohn–Sham equations were solved with the plane-wave pseudopotential method, as implemented in Vienna ab initio Simulation Package.<sup>18,19</sup> The  $k$ -mesh for sampling the Brillouin zone and plane-wave cutoff energy for expanding the electronic wave functions were chosen such that the total energies were converged within 0.65 meV/formula unit (f.u.). We chose  $U = 3.4$  eV, which produces the bandgap of M1 phase (0.7 eV) correctly.<sup>20</sup>

Figure 1 shows the phase transition driven by temperature under constant pressure (i.e., isobaric conditions). The pressure

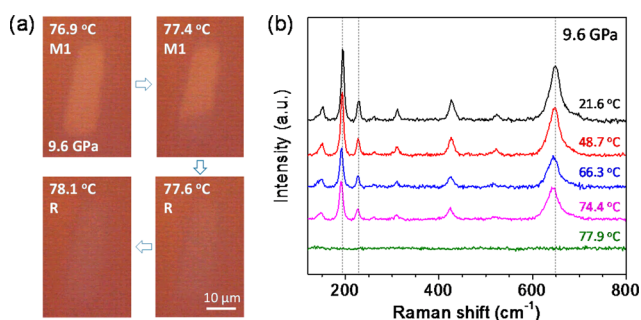


**Figure 1.** Phase transition of VO<sub>2</sub> driven by temperature under isobaric conditions. (a) Optical images of a VO<sub>2</sub> nanobeam across the M1–R phase transition at fixed pressure of 9.6 GPa. M1 and R phases show bright-yellow and dark-green contrast, respectively. (b) Raman spectrum evolving with temperature at the fixed pressure of 9.6 GPa.

was fixed at 9.6 GPa for experiments in Figure 1. As shown in Figure 1a, a sharp change in optical reflection is seen within a narrow temperature range ( $< \sim 0.2$  °C), signifying the transition from the insulating (bright) phase to the metallic (dark) phase, consistent with previous observations on this type of specimens.<sup>21,22</sup> The very narrow temperature range further confirms the nearly single-domain nature of the phase transition. This is also an indication that the specimens, which are transferred from the as-grown substrate to the diamond surface, sit loosely on the surface instead of being firmly clamped on it, and as such, any strain imposed by the diamond surface onto the specimen is negligible. The lack of strong clamping is also beneficial for the molecules of the

pressure medium to sip in underneath the sample, thus ensuring the hydrostaticity of the pressure transmitted to the sample. Raman spectra of the sample obtained at these temperatures are shown in Figure 1b. From the Raman spectrum, the low-temperature phase is clearly identified as the M1 phase. Combining isotope substitution and density functional theory calculations, it has been established that, in the M1 phase, the two low-frequency peaks of  $\omega = 193.9$  and  $228.5$  cm<sup>-1</sup> (at 21.6 °C) correspond to V–V lattice vibration, and all other Raman peaks are related to V–O vibration modes.<sup>23</sup> All of these modes slightly soften with increasing temperature, until reaching the transition temperature, above which all Raman peaks disappear owing to the metallicity of the R phase. The transition temperature obtained by Raman is identical with that obtained by optical reflection. More importantly, the transition temperature of  $T_{\text{MIT}} = 77.4$  °C at 9.6 GPa is higher than  $T_{\text{MIT}} = 68$  °C at ambient pressure ( $\sim 0$  GPa). This is consistent with previous report of a positive slope in the M1–R phase boundary.<sup>6</sup>

At constant temperature (i.e., isothermal condition), the hydrostatic pressure also drives VO<sub>2</sub> from the M1 phase to new phases. Shown in Figure 2a is the Raman spectra taken at fixed temperature of 50 °C with increasing pressure. The Raman peaks of the M1 structure gradually shift to higher wavenumbers with pressure, until very high pressure ( $\sim 33$  GPa) where they all disappear, indicating a metallic phase at and beyond that pressure. We mark this metallic phase as the X phase following previous work.<sup>9</sup> Plotting the pressure dependence of the three most prominent Raman peaks reveals new information, as shown in Figure 2b. It can be seen that the V–O mode at  $\omega = 617.5$  cm<sup>-1</sup> (2.5 GPa) blue shifts linearly with an initial rate of  $d\omega/dP = 4.1$  cm<sup>-1</sup>/GPa, but then the rate changes to a much shallower,  $2.4$  cm<sup>-1</sup>/GPa when the pressure is higher than 16.5 GPa. The two V–V modes, on the other hand, show no obvious change in the slope ( $d\omega/dP$ ). However, we note that, at lower temperatures such as room temperature (Supporting Information, Figure S2), these two V–V modes also show slight slope change at the same pressure where the V–O mode shows the slope change. This is consistent with previous, room-temperature pressure studies.<sup>7,23</sup> Therefore, before reaching the metallic phase, all of the M1 Raman modes remain, but some (or all, depending on temperature) of them show a change in the pressure rate at  $\sim 16.5$  GPa. This effect points to a continuous phase transition from M1 to a new, insulating M1' phase at this pressure, as suggested also by our previous room-temperature micro-X-ray diffraction (XRD)

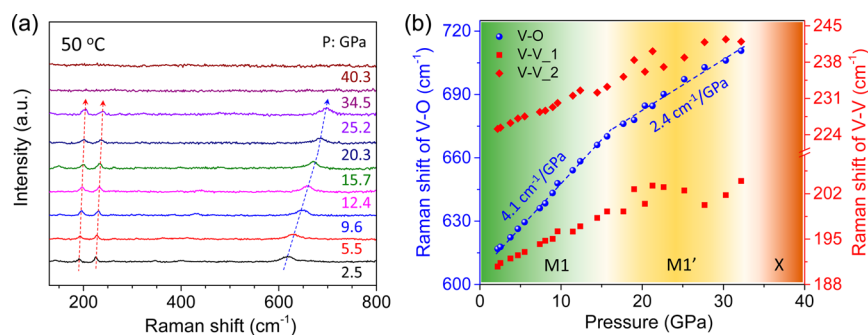


**Figure 2.** Phase transition of VO<sub>2</sub> driven by pressure under isothermal conditions. (a) Raman spectrum evolving from M1 to M1' and then X phase at fixed temperature of 50 °C. (b) Peak positions of different Raman modes as a function of pressure extracted from panel a.

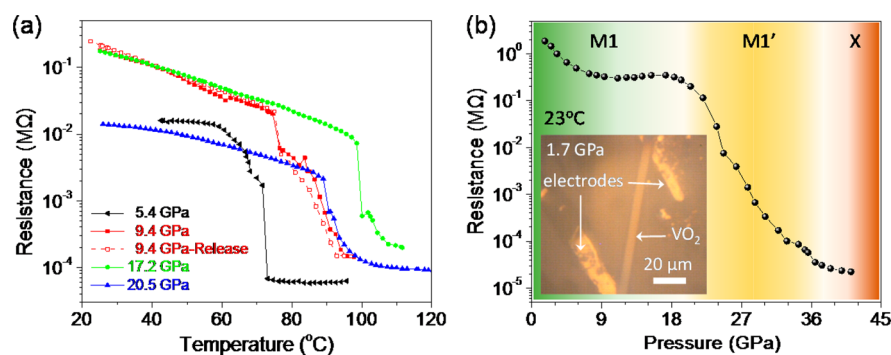


**Figure 3.** Electrical resistance of VO<sub>2</sub> across the phase transitions driven by temperature or pressure. (a) Temperature dependence of resistance of VO<sub>2</sub> under isobaric conditions. (b) Pressure dependence of resistance of VO<sub>2</sub> at room temperature. The inset is optical image of a quasi-four probe device for electrical measurements.

experiments.<sup>9</sup> The M1' phase is isostructural to M1, yet with very different electrical resistances as discussed below.

In order to probe the electronic nature of these phases, electrical transport measurements were also performed as a function of pressure or temperature. Figure 3a shows the resistance ( $R$ )–temperature ( $T$ ) dependence at fixed pressures. Similar to typical transport measurements at ambient pressure, at low temperatures VO<sub>2</sub> behaves as a doped semiconductor, with a decreasing resistance with temperature. At a certain temperature ( $T_{MIT}$ ), the resistance abruptly drops down by several orders of magnitude. The process is reversible, as cooling at the same pressure shows a very similar  $R$ – $T$  dependence with a small hysteresis as seen in Figure 3a. There are some small features on the  $R$ – $T$  curves, possibly attributed to inhomogeneous pressure in the DAC. The resistance was also measured as a function of pressure at room temperature, as shown in Figure 3b. A drastic change in the pressure dependence is seen in the range of 15–20 GPa, which is about the same pressure where the Raman peaks change slope in Figure 2b. Therefore, the much more rapidly decreasing resistance in Figure 3b is associated with the M1' phase. Such a new phase at high pressures has been considered as the onset of metallization process occurring in the monoclinic structure.<sup>7,24</sup> Our observation of the M1-like Raman peaks together with rapidly decreasing, yet nonmetallic, resistance in the M1' phase shows that it is still a monoclinic-structured insulating phase, but with a narrow bandgap rapidly closing from that of M1 phase ( $E_g \approx 0.7$  eV).<sup>20</sup> As pressure further increases beyond  $\sim 38$  GPa, VO<sub>2</sub> transforms into the metallic X phase showing very low resistance.

The optical reflectance, Raman, and electrical transport data obtained in isothermal and/or isobaric conditions allow us to construct a pressure–temperature phase diagram of VO<sub>2</sub>, including M1 (I), M1' (I), R (M), O (M), and X (M) phases as shown in Figure 4. Four phase transition points (black squares) obtained with micro-XRD at room temperature as well as 110 °C are also added for comparison.<sup>9</sup> It can be seen from Figure 4 that, although these data points were taken with different techniques (Raman, electrical, reflectance or XRD), along different axes of variables (isobaric or isothermal), and on different samples, they clearly define a consistent  $P$ – $T$  phase diagram over a wide pressure and temperature range. This phase diagram share some similarities to the largely schematic diagram of phases reported in ref 8: the  $P$ – $T$  phase boundary has a positive slope at low pressures, and evidence of new metallic phases at high pressures. However, the most striking features of this diagram are (1) the dome-like, nonmonotonic

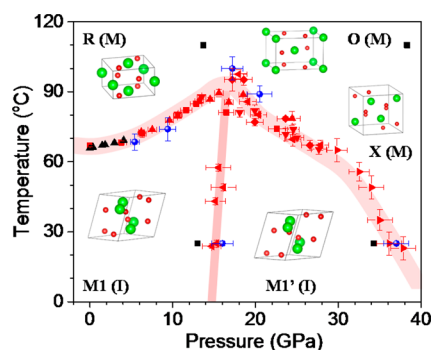


**Figure 4.** Phase diagram of VO<sub>2</sub> over a broad  $P$ – $T$  range, including M1 (I), M1' (I), R (M), O (M), and X (M). I and M represent insulating and metallic phases, respectively. Insets are the simulated atomic structures of each phases of VO<sub>2</sub> (V: green atoms, O: red atoms). The red and blue data points on the phase boundaries are obtained from Raman and electrical measurements, respectively, and different shapes of symbols represent different samples. The black square data points are determined by XRD extracted from ref 9. The black triangle data points are from ref 6. The error bars include the temperature and pressure uncertainties. The broad lines defining the phase boundaries are a guide to the eye.

phase boundary between the low-temperature, I phases and high-temperature, M phases (i.e., the MIT boundary), and (2) the gradual evolution along the pressure axis from the insulating M1 to the less insulating M1' and finally the metallic X phases, while the M1–M1' boundary incidentally extrapolates to the vertex of the MIT dome. In the following we analyze these features.

For the transition from the well-known M1 (I) to R (M), the slope of the phase boundary  $dT/dP$  is determined to be 1.4 °C/GPa when averaged over a wide range of  $P$  from 0 to 16 GPa. This is higher than the reported  $dT/dP = 0.8$  °C/GPa measured over  $P < 4$  GPa.<sup>6</sup> It can be seen from Figure 4 that the M1–R phase boundary takes a convex line shape, showing a higher slope at higher pressures. The M1–R transition is a first-order phase transition, with a discontinuous change in volume of  $\Delta V/V = 0.044\%$  at ambient pressure.<sup>25</sup> These quantities are related through the Clausius–Clapeyron equation  $dT/dP = T\Delta V/L$ , where  $\Delta V = V_R - V_{M1}$  is the molar volume change and  $L$  is the molar enthalpy change (latent heat) going from M1 to R. The positive slope ( $dT/dP$ ) is an indication of volume expansion going from M1 to R, consistent with reports.<sup>8,25</sup> Using the average  $dT/dP = 1.4$  °C/GPa and the ambient  $\Delta V/V = 0.044\%$ , an average  $L$  is calculated to be  $\sim 1.9$  kJ/mol,

compared to averaged value of  $L = 3.1\text{--}4.3$  kJ/mol in literature.<sup>25</sup>

By considering the  $P$  dependencies of  $dT/dP$  and  $\Delta V$ , it is possible to go beyond these averaged values and obtain values of  $L$  under pressure. The molar volume,  $V$ , has been experimentally measured as a function of  $P$  at 25 °C (M1 phase) and 110 °C (R phase) in ref 9, as well as a function of  $T$  (both M1 and R phases) at ambient pressure in ref 25, and these dependencies all appear linear within the range of pressure and temperature variations. Assuming that both  $V_{M1}$  and  $V_R$  depend on  $P$  and  $T$  following the linear functional form of  $\alpha P + \beta T + \delta$ , by fitting to the experimental data in refs 9 and 25, one can obtain  $\alpha_{M1}$ ,  $\beta_{M1}$ ,  $\delta_{M1}$  and  $\alpha_R$ ,  $\beta_R$ ,  $\delta_R$ . Consequently, the volume change  $\Delta V = V_R - V_{M1}$  is obtained as a function of  $T$  and  $P$ , and its values along the M1-R phase boundary is determined. Combining the values of  $\Delta V$  with the slope  $dT/dP$  of the measured phase boundary shown in Figure 4, the variation of  $L$  is obtained along the phase boundary. As shown in Figure S3c,  $L$  increases as a function of pressure, varying from 1.3 kJ/mol at ambient pressure to 12.2 kJ/mol at  $\sim 16$  GPa. Budai et al.<sup>26</sup> showed that the R structure is much more anharmonic than the M1 phase and that the total entropy change ( $0.43 k_B/\text{atom}$ ) across the MIT at ambient pressure is mostly attributed to softer anharmonic phonons in the R phase, rather than electronic contribution. Our discovery of increasing  $L$  points to even stronger lattice anharmonicity in the R structure at higher pressures.

We performed DFT calculations to investigate the M1'(I)–X(M) transition. The calculations for these phases covered pressures from 10 to 90 GPa as shown in Figure S4. By full optimization of the structure, the enthalpy and lattice parameters of the two phases were obtained. The volume is calculated to decrease by  $\sim 5\%$  from that of the M1' to X phase, which is much higher than that of the M1–R transition. As the slope  $dT/dP$  of the M1'–X phase boundary is negative with an averaged value on the same order of magnitude with that of the M1–R boundary, the average latent heat  $L$  is estimated to be positive going from M1' to X and much higher than  $L(\text{M1–R})$ , reaching  $\sim 155$  kJ/mol, suggesting a much higher entropy in the metallic X phase than in the metallic R phase.

For the M1 to M1' transition, the phase boundary is nearly vertical. We calculated the pressure-driven change in phonon frequencies using the finite difference method (see Figure S5). At  $P > 15$  GPa, some phonon modes start to deviate substantially in pressure dependency from those of the M1 phase. We evaluated the room-temperature Grüneisen parameters of the Raman modes,  $\gamma = -\partial \ln(\omega)/\partial \ln(V) = -(V/\omega)(d\omega/dP)/(dV/dP)$ . As shown in Figure S2, for the V–V Raman mode at  $222.1 \text{ cm}^{-1}$  (0 GPa),  $d\omega/dP$  increases from 0.2 for M1 to  $0.8 \text{ cm}^{-1}/\text{GPa}$  for the M1' phase, while for the V–O mode at  $608.2 \text{ cm}^{-1}$  (0 GPa), it decreases from 4.2 for M1 to  $1.7 \text{ cm}^{-1}/\text{GPa}$  for M1'. Using previous results of experimentally measured  $dV/dP$ ,<sup>9</sup> the obtained  $\gamma$  values exhibit an abrupt change at the M1–M1' transition pressure, with a sharp increase in  $\gamma(\text{V–V})$  and decrease in  $\gamma(\text{V–O})$ .

Finally, for the transition from the metallic R to the metallic O phase, calculations predict an onset of the transition in the range of 12–14 GPa (see Figure S6). As expected, the O phase comes with a gradually reduced volume (by 0.3% at 14 GPa and 2.2% at 30 GPa) as compared to the R-phase unit cell. Meanwhile, the  $a$ - and  $b$ -lattice parameters split into two values above the pressure for the tetragonal structure. Note that the absolute shifts of the atoms are even more pronounced, since

the oxygen parameters are given relative to the cell parameters and thus have to be multiplied by these in order to obtain the real distance between atoms. This R–O phase transition is also signaled by the difference of the enthalpies of the R and O phases as displayed in Figure S6a. The enthalpy calculated for the O structure starts to lower at about 13 GPa and then experiences a drastic drop between 15 and 30 GPa, thus stabilizing the O structure. We tried other functionals (PBE and PBEsol<sup>27</sup>) and found the same energy and structural relations between R and O phases.

In conclusion, we have experimentally mapped the phase diagram of VO<sub>2</sub> by independently varying pressure and temperature in a diamond anvil cell, which is also analyzed and supported by first-principles calculations. The diagram establishes phase boundaries not only between the well-known, insulating M1 phase and the metallic R phase, but also between the M1 phase and a more conductive M1' phase at intermediate pressures, as well as between the M1' phase and a metallic X phase at very high pressures. At high temperatures, the existence of another metallic O phase is also discussed. Our established phase diagram may serve as an instructive benchmark for ultimate elucidation of the phase transition physics of VO<sub>2</sub>, as well as its potential applications.

## ■ ASSOCIATED CONTENT

### 📄 Supporting Information

The Supporting Information is available free of charge on the ACS Publications website at DOI: 10.1021/acs.nanolett.7b00233.

Details of VO<sub>2</sub> growth and device fabrication in the DAC; Raman of a VO<sub>2</sub> nanobeam under isobaric heating; Raman during M1 to M1' transition driven by isothermal compression at room temperature; volume change and latent heat of M1–R transition; calculated M1' to X transition; calculated phonon frequencies as a function of pressure for the M1–M1' transition; calculated R–O transition; comparison of calculated enthalpy among M1, M1', R, O, and X phases at different pressures (PDF)

## ■ AUTHOR INFORMATION

### Corresponding Author

\*E-mail: wuj@berkeley.edu.

### ORCID

Kai Liu: 0000-0002-0638-5189

Junqiao Wu: 0000-0002-1498-0148

### Author Contributions

Y.C., S.Z., and F.K. contributed equally to this work.

### Notes

The authors declare no competing financial interest.

## ■ ACKNOWLEDGMENTS

This work was supported by U.S. NSF Grant No. 1608899. Y.C., J.W., and J.W.A. acknowledge support from the Singapore-Berkeley Research Initiative for Sustainable Energy (SinBeRISE). The laser milling was supported by BL12.2.2 at the Lawrence Berkeley National Laboratory and COMPRES (Grant No. EAR 11-57758). The authors acknowledge useful discussions with Dr. Hong Ding on DFT simulations and Dr. Wen Fan on DAC experiments.

## ■ REFERENCES

- (1) Morin, F. J. *Phys. Rev. Lett.* **1959**, *3* (1), 34–36.
- (2) Eyert, V. *Ann. Phys. (Berlin, Ger.)* **2002**, *11* (9), 650–702.
- (3) Yang, Z.; Ko, C. Y.; Ramanathan, S. *Annu. Rev. Mater. Res.* **2011**, *41*, 337–367.
- (4) Cao, J.; Ertekin, E.; Srinivasan, V.; Fan, W.; Huang, S.; Zheng, H.; Yim, J. W. L.; Khanal, D. R.; Ogletree, D. F.; Grossman, J. C.; Wu, J. *Nat. Nanotechnol.* **2009**, *4* (11), 732–737.
- (5) Neuman, C.; Lawson, A.; Brown, R. J. *Chem. Phys.* **1964**, *41* (6), 1591–1595.
- (6) Berglund, C. N.; Jayaraman, A. *Phys. Rev.* **1969**, *185* (3), 1034–1039.
- (7) Arcangeletti, E.; Baldassarre, L.; Di Castro, D.; Lupi, S.; Malavasi, L.; Marini, C.; Perucchi, A.; Postorino, P. *Phys. Rev. Lett.* **2007**, *98* (19), 196406–196409.
- (8) Marini, C.; Baldassarre, L.; Baldini, M.; Perucchi, A.; Di Castro, D.; Malavasi, L.; Lupi, S.; Postorino, P. *High Pressure Res.* **2010**, *30* (1), 55–59.
- (9) Bai, L. G.; Li, Q.; Corr, S. A.; Meng, Y.; Park, C.; Sinogeikin, S. V.; Ko, C.; Wu, J. Q.; Shen, G. Y. *Phys. Rev. B: Condens. Matter Mater. Phys.* **2015**, *91* (10), 104110.
- (10) Yajima, T.; Nishimura, T.; Toriumi, A. *Nat. Commun.* **2015**, *6*, 10104.
- (11) Hsieh, W. P.; Trigo, M.; Reis, D. A.; Artioli, G. A.; Malavasi, L.; Mao, W. L. *Appl. Phys. Lett.* **2014**, *104* (2), 021917–021921.
- (12) Zhang, X.; Zhang, J. K.; Ke, F.; Li, G. H.; Ma, Y. M.; Liu, X. Z.; Liu, C. L.; Han, Y. H.; Ma, Y. Z.; Gao, C. X. *RSC Adv.* **2015**, *5* (68), 54843–54847.
- (13) Guiton, B. S.; Gu, Q.; Prieto, A. L.; Gudiksen, M. S.; Park, H. J. *Am. Chem. Soc.* **2005**, *127* (2), 498–499.
- (14) Chen, Y.; Ke, F.; Ci, P.; Ko, C.; Park, T.; Saremi, S.; Liu, H.; Lee, Y.; Suh, J.; Martin, L. W.; Ager, J. W.; Chen, B.; Wu, J. *Nano Lett.* **2017**, *17*, 194.
- (15) Rekhii, S.; Dubrovinsky, L. S.; Saxena, S. K. *High Temp. - High Pressures* **1999**, *31* (3), 299–305.
- (16) Perdew, J. P.; Burke, K.; Ernzerhof, M. *Phys. Rev. Lett.* **1996**, *77* (18), 3865–3868.
- (17) Dudarev, S. L.; Botton, G. A.; Savrasov, S. Y.; Humphreys, C. J.; Sutton, A. P. *Phys. Rev. B: Condens. Matter Mater. Phys.* **1998**, *57* (3), 1505–1509.
- (18) Kresse, G.; Furthmüller, J. *Phys. Rev. B: Condens. Matter Mater. Phys.* **1996**, *54* (16), 11169–11186.
- (19) Blöchl, P. E. *Phys. Rev. B: Condens. Matter Mater. Phys.* **1994**, *50* (24), 17953–17979.
- (20) Fu, D. Y.; Liu, K.; Tao, T.; Lo, K.; Cheng, C.; Liu, B.; Zhang, R.; Bechtel, H. A.; Wu, J. Q. *J. Appl. Phys.* **2013**, *113* (4), 043707.
- (21) Wu, J. Q.; Gu, Q.; Guiton, B. S.; de Leon, N. P.; Ouyang, L.; Park, H. *Nano Lett.* **2006**, *6* (10), 2313–2317.
- (22) Liu, W. T.; Cao, J.; Fan, W.; Hao, Z.; Martin, M. C.; Shen, Y. R.; Wu, J.; Wang, F. *Nano Lett.* **2011**, *11* (2), 466–470.
- (23) Marini, C.; Arcangeletti, E.; Di Castro, D.; Baldassarre, L.; Perucchi, A.; Lupi, S.; Malavasi, L.; Boeri, L.; Pomjakushina, E.; Conder, K.; Postorino, P. *Phys. Rev. B: Condens. Matter Mater. Phys.* **2008**, *77* (23), 235111.
- (24) Marini, C.; Bendele, M.; Joseph, B.; Kantor, I.; Mitrano, M.; Mathon, O.; Baldini, M.; Malavasi, L.; Pascarelli, S.; Postorino, P. *Epl-Europhys. Lett.* **2014**, *108* (3), 36003.
- (25) Kucharczyk, D.; Niklewski, T. *J. Appl. Crystallogr.* **1979**, *12* (4), 370–373.
- (26) Budai, J. D.; Hong, J. W.; Manley, M. E.; Specht, E. D.; Li, C. W.; Tischler, J. Z.; Abernathy, D. L.; Said, A. H.; Leu, B. M.; Boatner, L. A.; McQueeney, R. J.; Delaire, O. *Nature* **2014**, *515* (7528), 535–539.
- (27) Perdew, J. P.; Ruzsinszky, A.; Csonka, G. I.; Vydrov, O. A.; Scuseria, G. E.; Constantin, L. A.; Zhou, X. L.; Burke, K. *Phys. Rev. Lett.* **2008**, *100* (13), 136406.

## ***Supporting information***

### **Pressure-Temperature Phase Diagram of Vanadium Dioxide**

Yabin Chen,<sup>1</sup> Shuai Zhang,<sup>2</sup> Feng Ke,<sup>3</sup> Changhyun Ko,<sup>1</sup> Sangwook Lee,<sup>1</sup> Kai Liu,<sup>4</sup>  
Bin Chen,<sup>3</sup> Joel W. Ager,<sup>1,5</sup> Raymond Jeanloz,<sup>2</sup> Volker Eyert,<sup>6</sup> and Junqiao Wu<sup>1,5,\*</sup>

1. Department of Materials Science and Engineering, University of California, Berkeley, CA 94720, USA.
2. Department of Earth and Planetary Science, University of California, Berkeley, CA 94720, USA.
3. Center for High Pressure Science and Technology Advanced Research, Shanghai 201203, China.
4. State Key Laboratory of New Ceramics and Fine Processing, School of Materials Science and Engineering, Tsinghua University, Beijing 100084, China.
5. Materials Sciences Division, Lawrence Berkeley National Laboratory, Berkeley, CA 94720, USA.
6. Materials Design SARL, 92120 Montrouge, France.

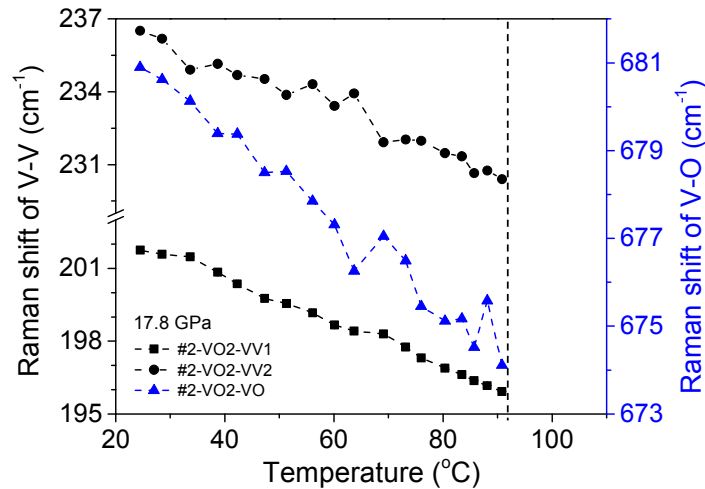
\*Corresponding author: [wuj@berkeley.edu](mailto:wuj@berkeley.edu)

Y.C., S.Z., and F.K. contributed equally to this work.

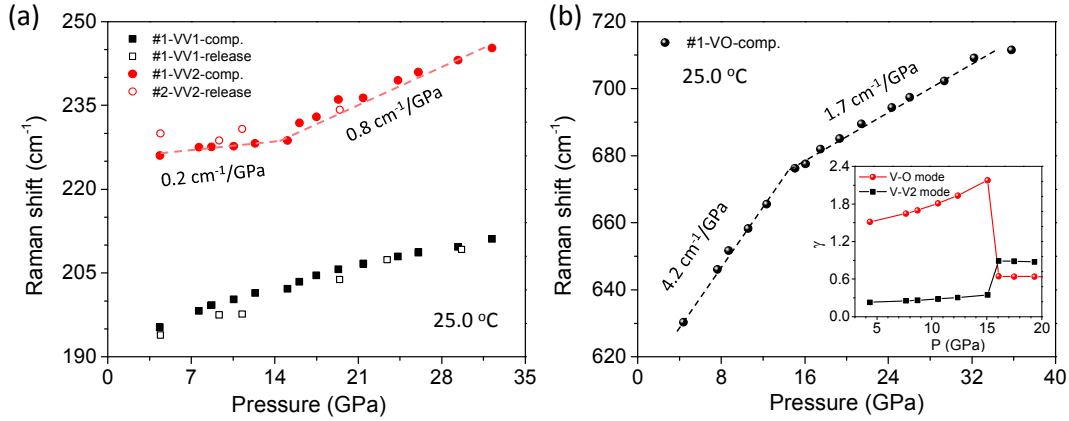
**Note.** VO<sub>2</sub> growth and device fabrication in the DAC.

The VO<sub>2</sub> nanobeams were grown in a low-pressure horizontal quartz tube furnace by chemical vapor transport method. The unpolished quartz (~1 cm×0.6 cm) was used as substrate. In brief, V<sub>2</sub>O<sub>5</sub> precursor was placed in a quartz boat, and its distance from quartz substrate was ~1.5 cm. The furnace was then heated to 950 °C. The evaporated precursor was transported by Ar gas (6.8 sccm, 4.0 Torr), and then formed VO<sub>2</sub> nanobeams on quartz surface. After 15 min, the system naturally cooled down to room temperature.

The device fabrication and measurements were performed in a four-post DAC with 300 μm culet size. The steel gasket was coated by a mixed powder of cubic-boron nitride and epoxy to electrically isolate different electrodes, and the final gasket hole drilled by laser was about 100 μm as the sample chamber. Daphene 7373 oil was utilized as the pressure transmitting medium. Pt strips (~5 μm thickness) cut by a sharp blade were used as electrodes. A VO<sub>2</sub> nanobeam was transferred from the as-grown quartz substrate to the diamond surface by a probe tip. A ruby particle was placed near the VO<sub>2</sub> nanobeam as the pressure sensor. Electrical connections between Pt electrodes and VO<sub>2</sub> were achieved using silver paste. An optical image of the fabricated device is shown in the inset of Figure 3b.

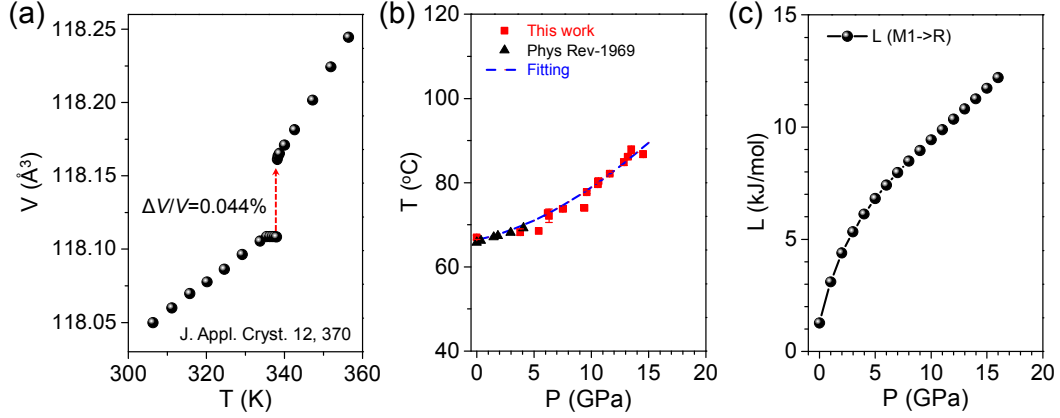


**Figure S1. Isobaric heating of VO<sub>2</sub> nanobeam at  $P = 17.8$  GPa.** All three Raman peaks red-shift as temperature increases without discernible feature on the curve. When the temperature reaches ~90.8 °C, all Raman peaks disappear abruptly, indicating entering a new metallic phase.



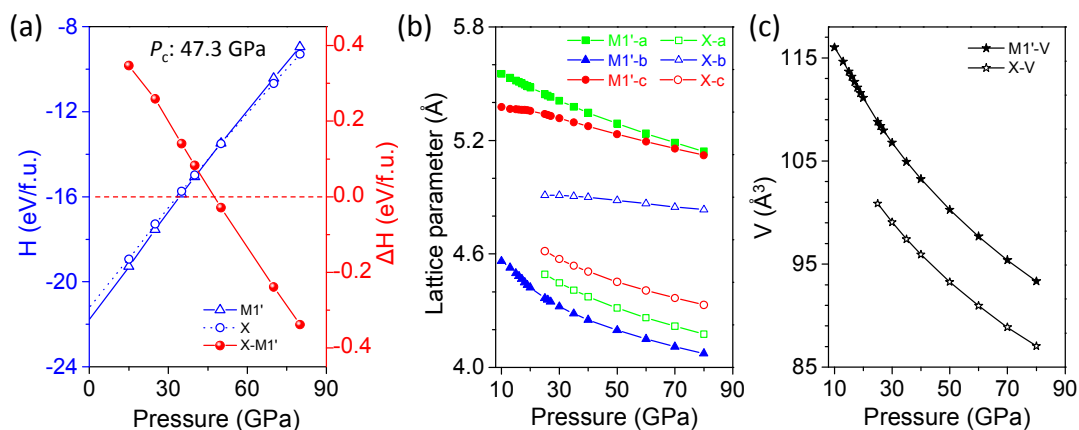
**Figure S2. Raman shifts during the M1 to M1' transition driven by isothermal compression at room temperature.** (a) Raman shifts of the two V-V modes at different pressures. The solid and hollow symbols indicate data obtained at the compressing and pressure-releasing process, respectively. (b) Pressure dependence of the V-O vibration Raman mode. The slope of  $d\omega/dP$  on the curves before and after the phase transition was also labelled. Inset in (b) is the Grüneisen parameter ( $\gamma$ ) of the two modes as a function of pressure.

Figure S2 shows the pressure-dependent Raman shift during the M1 to M1' transition. As the pressure increases, both the V-V and V-O modes stiffen. The slope of the V-V2 mode changes from 0.2 to 0.8 cm<sup>-1</sup>/GPa at the M1 - M1' transition, while the slope of the V-O decreases from 4.2 to 1.7 cm<sup>-1</sup>/GPa. Furthermore, we calculated the pressure-dependent Grüneisen parameters ( $\gamma$ ) of the V-O and V-V2 modes using  $\gamma = -\partial \ln(\omega) / \partial \ln(V) = -(V/\omega_i)(d\omega_i/dP)/(dV/dP)$ , as shown in the Inset of Figure S2b. Both Grüneisen parameters show an abrupt change at 15.1 GPa, the M1 - M1' transition pressure. The phonon Grüneisen parameter is a measure of the anharmonicity of the lattice vibration mode. Both the Grüneisen parameters increase with pressure in the M1 phase, indicating enhanced anharmonicity by pressure. Across the M1 to M1' transition,  $\gamma(V-V2)$  increases and  $\gamma(V-O)$  decreases. The increase in  $\gamma(V-V2)$  is an indication of drastically enhanced anharmonicity along the V-V chain when going from M1 to the M1' phase.



**Figure S3. M1 to R transition.** (a) Experimentally measured unit cell volume change of VO<sub>2</sub> adopted from Ref. 25 [J. Appl. Crystallogr. 12, 370 (1979)] used to calculate the latent heat. Note that the volume expands by 0.044% during the M1 - R transition at ambient pressure. (b) Polynomial fitting of the M1-R phase boundary. Red points are data obtained in this work, and black points are from Ref. 6 [Phys. Rev. 185, 1034 (1969)]. (c) The calculated pressure-dependent latent heats along the M1-R boundary.

Following the Clausius-Clapeyron equation for first-order transitions, the latent heat  $L = T \times \Delta V / (dT/dP)$ , where  $\Delta V$  is the molar volume change across the transition, and  $dT/dP$  is the slope of the phase boundary. In both the M1 and R phases, the molar volume depends on both temperature and pressure. After linearly fitting the experimentally reported volume at different  $T$  and  $P$  (Refs. 9 [Phys. Rev. B 91, 104110 (2015)] and 25 [J. Appl. Crystallogr. 12, 370 (1979)]) using  $V_{M1} = \alpha_{M1} \times (T-25) + \beta_{M1} \times P + \delta_{M1}$ , and  $V_R = \alpha_R \times (T-110) + \beta_R \times P + \delta_R$ , we obtain  $\alpha_{M1} = 0.0018 \text{ \AA}^3/4\text{f.u./}^\circ\text{C}$ ,  $\beta_{M1} = -0.47 \text{ \AA}^3/4\text{f.u./GPa}$ ,  $\delta_{M1} = 118.11 \text{ \AA}^3/4\text{f.u.}$ , and  $\alpha_R = 0.0048 \text{ \AA}^3/4\text{f.u./}^\circ\text{C}$ ,  $\beta_R = -0.44 \text{ \AA}^3/4\text{f.u./GPa}$ ,  $\delta_R = 118.40 \text{ \AA}^3/4\text{f.u.}$ . Next, we fit the M1-R boundary in the  $T - P$  diagram by  $T = A \times P^3 + B \times P^2 + C \times P + D$  as shown in Figure S4b, and obtain A, B, C, and D as  $-0.00068 \text{ }^\circ\text{C/GPa}^3$ ,  $0.075 \text{ }^\circ\text{C/GPa}^2$ ,  $0.56 \text{ }^\circ\text{C/GPa}$ , and  $66.44 \text{ }^\circ\text{C}$ , respectively. As shown in Figure S3c, the thus calculated  $L$  increases monotonously with pressure.



**Figure S4. Calculation of M1' to X transition at zero Kelvin temperature.** (a) Calculated pressure-dependent enthalpy of M1' and X phases and their difference. Their crossing point indicates a transition pressure of  $\sim 47$  GPa. (b-c) Simulated lattice parameters (b) and volume (c) of M1' and X phases as a function of pressure. At 47GPa, all lattice parameters ( $a$ ,  $b$ , and  $c$ ) and volume show a discontinuous transition from the M1' to X phase. The relative volume change is  $\sim 5\%$ .

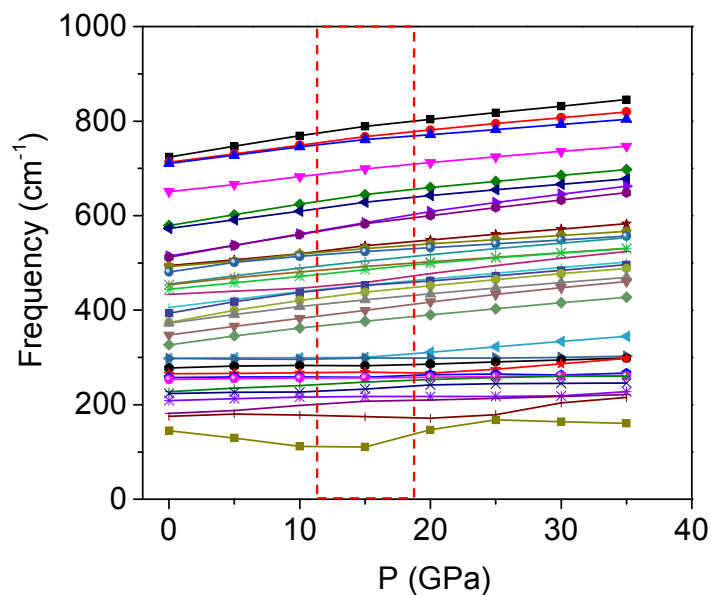


**Figure S5. Calculated phonon frequencies at the Brillouin-zone center as a function of pressure for the M1 - M1' transition at zero Kelvin temperature.** It can be seen that some phonon modes split or change slope at 12~18 GPa (red box).

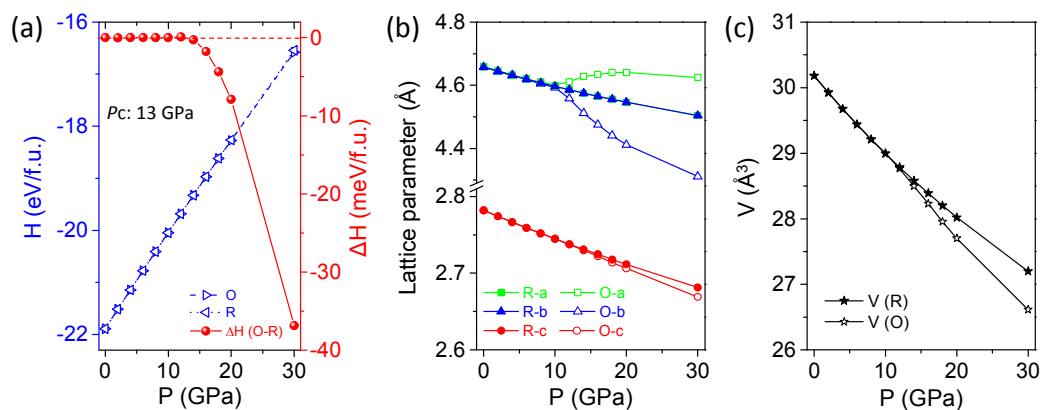


**Figure S6. Calculated R to O transition at zero Kelvin temperature.** (a) Calculated pressure-dependent enthalpy of R and O phases and their difference. The transition occurs at  $\sim 13$  GPa. (b-c) Simulated lattice parameters (b) and volume (c) of R and O phases as a function of pressure.

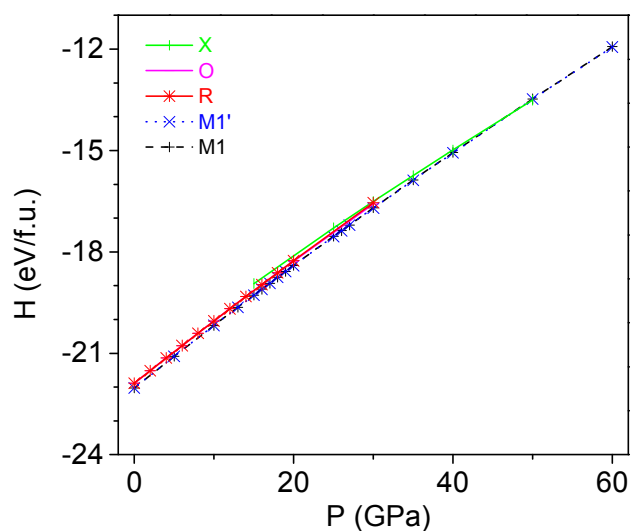


**Figure S7. Comparison of calculated enthalpy between M1, M1', R, O, and X phases at different pressures (zero Kelvin temperature).** It is seen that generally the insulating phases (M1 and M1') show lower enthalpy than the metallic phases (R, O, and X) at the same pressure.